

# Development and Testing of a Minaturized, Dual-Frequency GPS Receiver for Space Applications

Andrew J. Joplin, *The University of Texas at Austin*  
E. Glenn Lightsey, *The University of Texas at Austin*  
Todd E. Humphreys, *The University of Texas at Austin*

## BIOGRAPHIES

Andrew J. Joplin is a graduate student in the department of Aerospace Engineering and Engineering Mechanics at the University of Texas at Austin. He received a B.S. in Aerospace Engineering, with an emphasis on Space Flight, from the University of Texas at Austin. His interests are in the areas of orbital mechanics, orbit determination, and GNSS technology and applications.

E. Glenn Lightsey is a professor in the Department of Aerospace Engineering and Engineering Mechanics at the University of Texas at Austin. He received a B.S.E. from Princeton University, an M.S. from The Johns Hopkins University, and a Ph.D. from Stanford University. His research involves small satellite technology, including: guidance, navigation, and control; attitude determination and control; formation flying, satellite swarms, and satellite networks; cooperative control; proximity operations and spacecraft rendezvous; space based GNSS; visual navigation; propulsion; satellite operations; and space systems engineering.

Todd E. Humphreys is an assistant professor in the department of Aerospace Engineering and Engineering Mechanics at the University of Texas at Austin. He received a B.S. and M.S. in Electrical and Computer Engineering from Utah State University and a Ph.D. in Aerospace Engineering from Cornell University. His research interests are in estimation and filtering, GNSS technology, GNSS-based study of the ionosphere and neutral atmosphere, and GNSS security and integrity.

## ABSTRACT

Dual-frequency space-based GPS receivers have many mission-enabling capabilities as compared to their single-frequency counterparts. The ionosphere-corrected range measurement allows precise orbit determination (POD) of the spacecraft to centimeter level, which has been successfully demonstrated in several space missions that have studied the Earth. Furthermore, the dual-frequency measurement allows observation of the ionospheric delay, which supports GPS radio occultation and space weather experiments. With the emergence of a second civilian GPS signal, dual-frequency measurements may be used for future real-time space applications such as autonomous formation flying, satellite networks, and cooperative control (e.g., satellite inspection and rendezvous).

While dual-frequency GPS receivers have been used in space for more than two decades, the size, power, and cost of this technology is an important driver for future space missions. The growing availability of launch opportunities for very small satellites known as nanosatellites and CubeSats raises the possibility of more affordable access to space measurements if the observation quality is sufficient to support the user's needs.

This paper presents the initial development and testing of the Fast, Orbital, TEC, Observables, and Navigation (FOTON) receiver: a small, reconfigurable, dual-frequency, space-based GPS receiver. Originally developed as a science-grade software receiver for monitoring ionospheric scintillation and total electron content (TEC), this receiver was designed to provide high-quality GPS signal observations. The original receiver hardware was miniaturized and the software has been adapted for low earth orbit (LEO) operations. FO-

TON now fits within a 0.5U CubeSat form factor (8.3 x 9.6 x 3.8 cm), weighs 400 g, and consumes 4.5 W of instantaneous power, which can be reduced to  $\mu$ 1 W orbit average power with on-off duty cycling. The receiver has been designed with commercial parts to keep manufacturing costs low.

Significant testing of FOTON has been performed with live signals and with signals generated by a Spirent GPS signal simulator. Initial terrestrial tests demonstrate behavioral consistency with the original heritage high performance receiver. Several LEO simulations are presented, demonstrating FOTON's single- and dual-frequency positioning, Kalman filter based POD, and GPS radio occultation observation capabilities. In addition, its acquisition and reacquisition performance is presented; on average, FOTON's time to first fix is approximately 45 seconds. Finally, an orbital Kalman filter is introduced to enable navigation in geostationary orbit (GEO), which is a challenging application for space-based GPS navigation. Extensive testing demonstrates that FOTON is a robust, versatile, high-precision dual-frequency space receiver. Its low cost, size, weight, and power requirements are key enablers for future small-satellite missions.

## 1 INTRODUCTION

The position, velocity, and timing (PVT) requirements for satellites varies according to the mission. Some satellites, such as some of the student-built CubeSats developed by the University of Texas at Austin (UT-Austin) Satellite Design Laboratory, require only very coarse navigation capability. Major space science missions, however, often require precise (sub-meter) navigation. One example is the Gravity Recovery and Climate Experiment (GRACE), which uses K-band range measurements to detect changes in Earth's local gravitational field [1]. This requires high-precision knowledge of the GRACE satellites' positions. Some small satellite missions (such as FASTRAC [2]) involve relative navigation of two satellites, and could lead to automated rendezvous and docking demonstrations. The higher precision required for such goals can be attained using dual-frequency GPS receivers.

Another use for dual-frequency receivers on satellites is ionospheric research. A typical ionospheric research mission, such as the Constellation Observing System for Meteorology, Ionosphere, and Climate (COSMIC) mission [3], involves relatively large, expensive satellites. If such a mission could be accomplished using CubeSats, the science return per dollar spent would

be significantly higher.

This paper focuses on such navigation and scientific applications of space-based GPS receivers, with special attention given to small satellite applications. It presents a small, dual-frequency receiver that is under development, and is expected to be the primary navigation sensor on UT's upcoming ARMADILLO mission. The Fast, Orbital, TEC, Observables, and Navigation (FOTON) receiver (Fig. 1) is a miniaturized version of a dual-frequency terrestrial science receiver developed by Cornell University and The University of Texas at Austin.

As part of this research, changes have been made to FOTON's software to allow it to navigate in the more challenging environment of space. Some additions have also been made to the software to improve its performance, including an orbital Kalman filter to supplement the existing point solution algorithm. The results of considerable testing are also presented to demonstrate FOTON's capabilities in a variety of scenarios, including both static and simple dynamic terrestrial tests, single- and dual-frequency low Earth orbit (LEO) tests, and a geosynchronous orbit (GEO) test.



**Figure 1** FOTON Receiver

The next section presents a brief overview of software receivers in general, and FOTON specifically. It also summarizes the major changes that needed to be made in order for FOTON to navigate on orbit, most of which were either discovered or verified by the testing presented in Section 3. In addition to describing the setup and procedures used in testing FOTON, Section 3 presents the results of the initial characterization of the CASES and FOTON receivers, comprising a live-sky test, static and dynamic terrestrial simu-

lations, and two LEO simulations. Section 4 examines FOTON’s signal acquisition and reacquisition performance as a precursor to an in-depth duty cycling study. This is followed in Section 5 by a description of a LEO extended Kalman filter designed by the author. This filter provides a core capability that can be later improved to make possible sub-meter precision orbit determination. Section 6 presents the results of the initial dual-frequency LEO simulation testing; it compares several single- and dual-frequency configurations to illustrate FOTON’s dual-frequency navigation performance. This is followed by a brief overview of radio occultation and an example of how FOTON can be used to measure entire local ionospheric delay profiles. Finally, Section 8 demonstrates FOTON’s navigation capability in a geosynchronous orbit simulation, an accomplishment made possible through the use of a high-precision timing reference and the reconfigurability of a software receiver.

## 2 BACKGROUND

FOTON is a dual-frequency, software-defined GPS receiver adapted from the Connected Autonomous Space Environment Sensor (CASES) receiver developed by Cornell University and The University of Texas at Austin. The CASES receiver consists of a radio frequency (RF) front end, a single-board computer (SBC), and a digital signal processor (DSP) chip. The software that runs on CASES is the GNSS Receiver Implementation on a DSP (GRID) code, written in C++. FOTON, the space-based version of the receiver, uses the same hardware as CASES, repackaged to fit within a 0.5U CubeSat volume (approximately 8.3×9.6×3.8 cm). FOTON runs an altered version of the GRID code that was developed in this research and works in low earth orbit. This section discusses the advantages of software receivers in general, and provides a brief overview of the original GRID code, the CASES receiver, and FOTON. A summary of the changes required to make FOTON function in LEO is also provided.

### 2.1 Software Receivers

Traditional GPS receivers are composed of general-purpose processors and application-specific integrated circuits (ASICs). The signal correlation is performed on ASICs, while tracking and navigation are performed on the processor. This is acceptable in most cases, because there is often no reason to make changes to

the receiver. Software-defined receivers, however, ingest raw digital signals from a data acquisition (DAQ) board and perform correlation as well as tracking and navigation on a general-purpose processor.

Software-defined receivers have recently been gaining popularity due to the ease with which any part of the receiver, from navigation all the way down to correlation, can be changed. This allows for significantly decreased development time, as well as greater receiver customization. When considering space-based GPS receivers, this advantage becomes even more pronounced; if a bug is found in the receiver when it is already on-orbit, or if additional functionality is desired, the same satellite may still be used by simply uploading new software to the receiver. As will be demonstrated in Chapter 8, the ability to make changes to a receiver’s correlation opens up the possibility of using a single receiver design for geosynchronous orbit positioning in addition to terrestrial and low Earth orbit positioning. While it is true that software receivers, in general, have higher power requirements than their hardware-based counterparts, the recent advancements in microprocessor technology renders this disadvantage insignificant compared with the flexibility offered by software receivers.

### 2.2 GRID Code

The GRID code processes a stream of binary, intermediate frequency (IF) sign, magnitude, and clock data from an RF front end, tracking GPS L1 C/A and L2C signals, and producing a navigation solution (see Fig. 2). The data can be input to a DSP in real-time from the front end, or it can be recorded and used as input to the equivalent post-processing receiver (PpRx). PpRx is a post-processing implementation of GRID, designed to be compiled and run on any Linux computer. It shares most of the same code as the real-time, DSP-based receiver, so the only difference in behavior should be run-time speed.

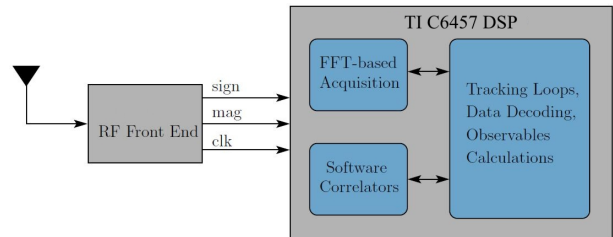


**Figure 2** Schematic Representation of GRID [4]

The GRID code is designed to take advantage of the object-oriented programming capabilities of C++.

Signal tracking is handled by two main classes: **Bank** and **Channel**, both fully configurable. The **Bank** class contains all of the information required for tracking a specific signal type, such as L1 C/A or L2C. Although GRID is capable of tracking other signal formats, such as L5 and other CDMA signals, this report will focus on L1 C/A and L2C only. The **Channels** contain loop and observables information for each signal being tracked within a **Bank**.

### 2.3 CASES and FOTON Receivers

The CASES receiver is constructed from commercial, off-the-shelf (COTS) components on custom-built circuit boards (Fig. 3). The FOTON receiver is a miniaturized version of CASES (Fig. 1). It consists of three boards:



**Figure 3** CASES Receiver in Two Form Factors [5]

- RF Front End
- Digital Signal Processor (DSP)
- Interface Board (Z-board)

The RF front end, developed by Dan Bobyn Engineering, Ltd., down-converts L1 and L2 signals to an intermediate frequency of 298.73 MHz, samples at 5.714286 MHz, and quantizes the digital signal using two-bit quantization (sign and magnitude) [6]. It accepts a single antenna input, as well as an optional external clock reference input. In the absence of an external clock reference, the front end uses an internal Temperature-Controlled Crystal Oscillator (TCXO).

The quantized digital signal is then fed into a reprogrammable, 1 GHz Texas Instruments C6457 DSP board for processing [7]. The DSP, using the GRID code described in the previous section, is responsible for acquiring and tracking GPS L1 and L2 signals, computing pseudorange, Doppler, and carrier phase observables, and computing a navigation solution from the observables. The processed channel data, along with the navigation solution, are then output through the Z-board to a satellite's on-board computer.

#### *Software Changes*

Because the GRID software was originally designed to run on a static, terrestrial receiver, several fundamental changes needed to be made before it could be used on FOTON. These software changes, like the hardware reconfiguration, were also made by the Radionavigation Laboratory.

The first change that needed to be made was widening the Doppler search window. Terrestrial receivers with TCXOs typically see up to 6 kHz Doppler, caused by the motion of the GPS satellite and the drift rate of the receiver's TCXO. The Doppler observed by receivers in LEO, however, is dominated by the receiver's dynamics, and can be as high as 40 kHz. Without widening the Doppler window, FOTON would not be able to track signals in LEO.

Another important change was in the navigation solution algorithm; because GRID was designed for static receivers, it uses a position averaging filter to attain sub-meter level accuracy. This must be turned off, however, for any dynamic scenarios, including LEO. Several other changes were made to the GRID in the process of making it space-capable, but as they were more general updates only indirectly related to FOTON, they will not be discussed.

### 3 CHARACTERIZATION OF CASES AND FOTON

This section presents the initial characterization and development testing of the CASES and FOTON receivers. This not only illustrates how tightly coupled testing and development were in the project, but it also provides proper perspective for understanding the results of testing presented in later sections. First, an overview of the testing setup and procedures is given, including a brief description of the hardware. Next, the results of testing the CASES receiver are presented; these act as a baseline for evaluating the

performance of changes made to the code during early FOTON development. Finally, the initial characterization of the FOTON receiver is presented. The last test in this section is a recreation of the LEO benchmark test developed by Holt [8]. Thanks to the previously documented results of this same test on other receivers [9], FOTON’s performance can be directly compared with other space-based receivers.

### 3.1 Setup and Procedures

There are two basic types of tests that were performed: live sky tests and simulations. Although some live sky testing is presented to verify that the receiver does, in fact, work properly with live data, the majority of testing presented used simulated signals. Simulations comprise static terrestrial, dynamic terrestrial, low earth orbit, and high earth orbit/geosynchronous (GEO) tests.

#### *Live-Sky Testing*

The live sky tests were conducted using a static GPS antenna on the roof of the W. R. Woolrich Laboratories building at the University of Texas at Austin. The signals were transmitted via coaxial cable to the CASES receiver, and the output from CASES was transmitted to a separate computer for analysis.

#### *Simulator Setup*

The Spirent GPS signal simulator is located at the Center for Space Research (CSR) GPS laboratory, and can be set up to simulate a variety of scenarios, from a stationary receiver to a receiver in orbit. The simulation scenario is defined on an adjacent computer. Different parameters can be varied, including simulated antenna gain patterns and GPS constellation parameters. The simulator can also simulate atmospheric effects, such as ionospheric and tropospheric delay. The tests presented in this section, however, have these effects turned off. The intent is to test the receiver’s base performance to compare with other receivers. The simulator also saves a log file containing the simulated position, velocity, and time, as well as satellite position and observables.

The output of the simulator is the (nearly) analog signal that would be output from a receiver antenna, as defined in the simulation scenario. A coaxial cable connects the simulator’s RF output to the receiver’s antenna input. A coaxial splitter is also used to input

the same signal to a device called a “bitgrabber”. The bitgrabber consists of a Bobyn front end (the same as FOTON’s front end) connected to an Acces-IO USB-DI16A data acquisition board [10]. This board transmits the digitized IF data from the front end through USB to a computer or hard drive for storage. Recording simulations in this way allows for quick testing of changes to the software without having to go back to CSR’s GPS lab to re-run the tests.

### 3.2 CASES Receiver Testing

Before presenting the results of the FOTON characterization, three tests on the CASES receiver are presented: a live-sky test, a static simulation, and a LEO simulation.

#### *Live-Sky Test*

Approximately 20 minutes of live-sky data was recorded using the CASES receiver with the default GRID configuration. The average position and velocity over the 20 minute interval is subtracted to obtain approximate position and velocity residuals, shown in the following two figures.

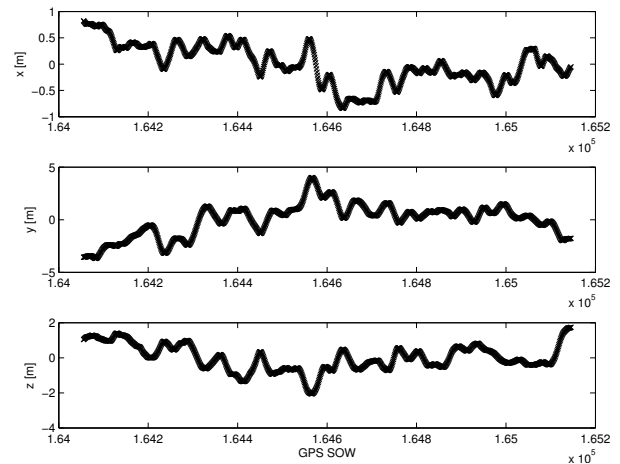


**Figure 4** CASES Live-Sky Position Residuals

The default GRID configuration uses a position averaging filter to improve position precision over time; the effect of this filter is seen in Figure 4 as the position residuals “walk”, rather than exhibiting Gaussian variations as do the velocity residuals (Fig. 5). The non-Gaussian behavior of the position residuals could alternatively be explained by multipath or some other time-correlated phenomenon; however, the averaging filter would most likely dominate other such effects. The 1- $\sigma$  error in position and velocity is summarized

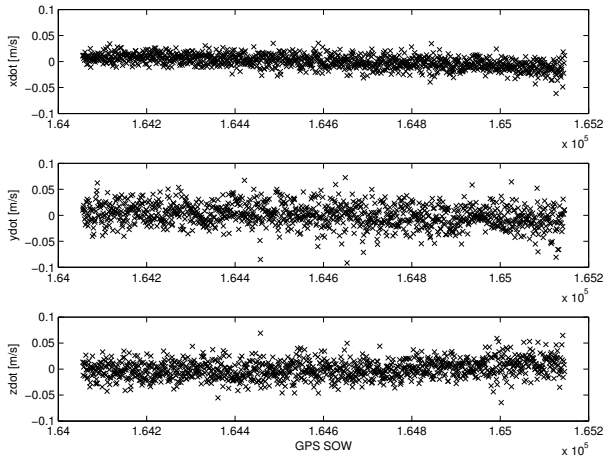


**Figure 5** CASES Live-Sky Velocity Residuals

in Table 1. After only 20 minutes, the positioning error was less than 2 meters. Greater precision is possible with longer position averaging times.

**Table 1** CASES Live-Sky 1- $\sigma$  Error

	X	Y	Z	$\  \cdot \ $
Position [m]	0.377	1.541	0.744	1.753
Velocity [m/s]	0.013	0.022	0.017	0.031

### Static Test

The static simulation scenario simulated the receiver at 30° N, 97° W, and included both ionospheric and tropospheric delays. Like the live sky test, the CASES receiver was used with the default GRID configuration, including the position averaging. Figure 6 shows the position filter converging toward the true solution over the course of the 2-hour simulation. The spikes in the plot result from changes in the tracked GPS satellites, which can be seen as changes in position dilution of precision (PDOP). Also shown in this figure is the ratio of RMS error to PDOP, which is normally used to calculate user range error (URE). However, URE is based on the assumption of a normally-distributed position error; because of the position filtering, URE cannot be calculated.

### LEO Test

The purpose of this test was to see how the GRID code, without any changes from the default configuration, would perform in a LEO scenario. The simulator was set up with a typical 90 minute low earth orbit (specifically that of the International Space Station [11]), and the simulation logging set to record the observables for all GPS satellites simulated. As expected, the receiver was not able to track enough

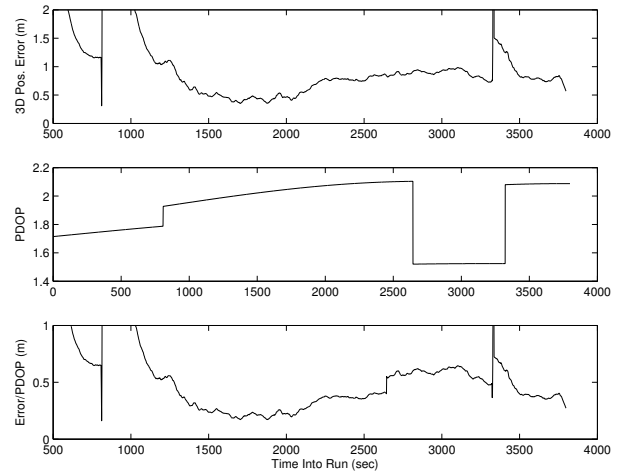


**Figure 6** CASES Static Simulation RMS Error and PDOP

satellites to obtain a navigation solution; however, it was able to track 1-3 satellites at a time. The primary tracking constraint was Doppler: GRID, by default, can only track Doppler on the range of +/- 10 kHz (see Fig. 7). Contrast this figure with the actual Doppler simulated (Fig. 8); the actual simulated Doppler is on the range of +/- 40 kHz.

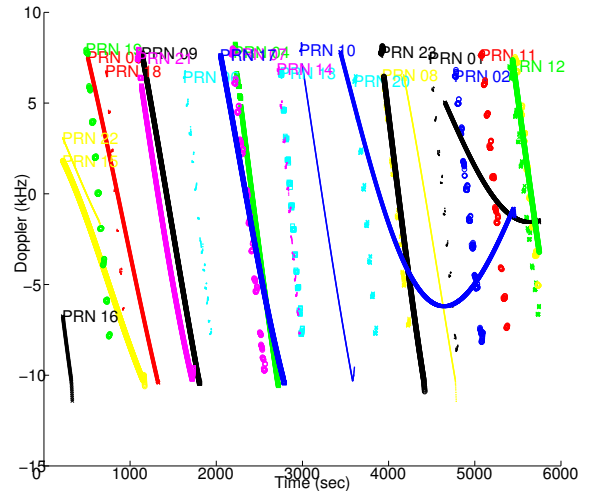


**Figure 7** LEO Tracked Doppler History

### 3.3 FOTON Receiver Testing

After some required software changes to GRID, including the widening of the Doppler tracking window, the FOTON receiver was ready for testing. The first two tests were terrestrial: a static simulation and a simple rectangular track simulation. These tests were intended to verify that FOTON performed as expected

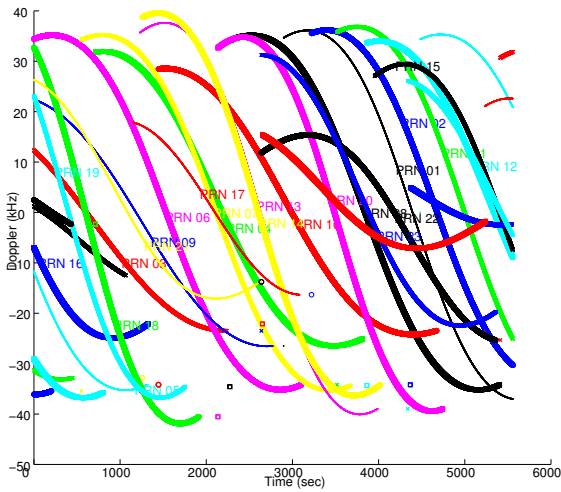


Figure 8 LEO Simulated Doppler History

for a terrestrial receiver before attempting LEO positioning. These tests revealed a difference between the real-time receiver and PpRx, uncovering a bug in the SBC code, which was quickly located and fixed. Once the real-time receiver performed the same as PpRx, the code could be tested using an established LEO benchmark test. This test allows FOTON to be directly compared with other space-based GPS receivers, including the Orion single-frequency receiver used by small satellites in the past and the Jet Propulsion Laboratory’s (JPL) dual-frequency BlackJack receiver, which has previously been used in major science missions.

**Static Test**

The static test was a repeat of the CASES static simulation, but without the atmospheric delays. Because this test is only used to demonstrate the basic functionality of the receiver, it was only 15 minutes long. The position and velocity residuals from the static simulation are shown in Figure 9. There was a 0.41 m overall bias in position, with a 0.46 m standard deviation. The velocity was zero-mean, with a 1- $\sigma$  error of 0.035 m/s.

**Rectangular Track Test**

The rectangular track test simulated the receiver traveling around a terrestrial track at velocities and accelerations of a typical car. This test demonstrates FOTON’s capabilities to accurately track a receiver undergoing relatively slow terrestrial dynamics. Figure 10 shows the simulated trajectory in ECEF coordinates.

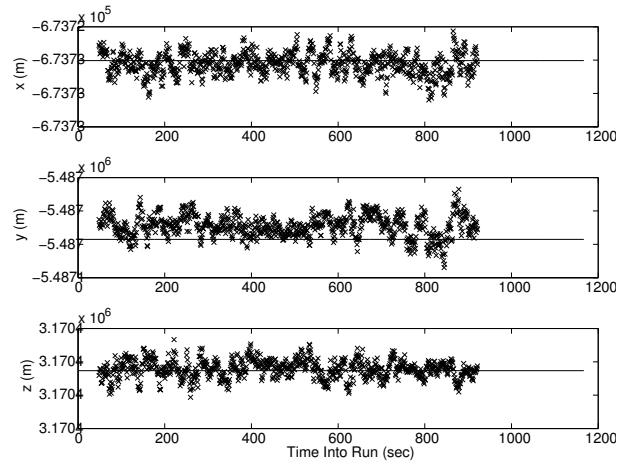


Figure 9 FOTON Static Simulation Residuals

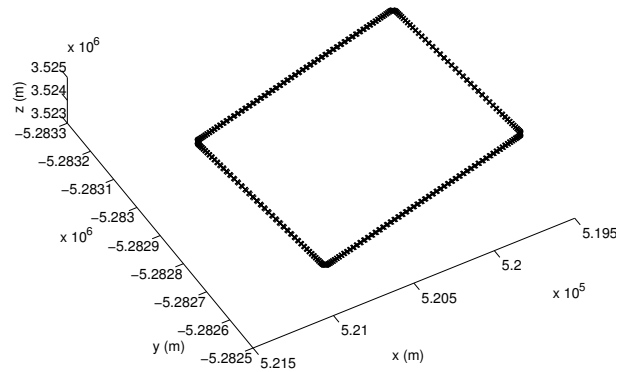


Figure 10 FOTON Rectangular Track Trajectory

The RMS position and velocity errors are shown in Figure 11. Both position and velocity were nearly zero-mean, with 1- $\sigma$  errors of 0.83 m and 0.12 m/s, respectively.

**LEO Benchmark Tests**

In 2002, Holt developed a LEO simulation specifically designed to test receiver performance under a variety of relative dynamics and signal levels [8]. The 2 hour simulation consists of a nearly polar orbit containing six pairs of GPS space vehicles (SVs) specifically chosen according to their relative dynamics and signal levels. This simulation uses L1 C/A only, and does not simulate ionospheric or tropospheric effects. It also does not include any ephemeris errors. By removing these sources of error, this simulation makes possible an analysis of raw observable noise.

The analysis consists of a series of double difference calculations using specified pairs of SVs and the “true”

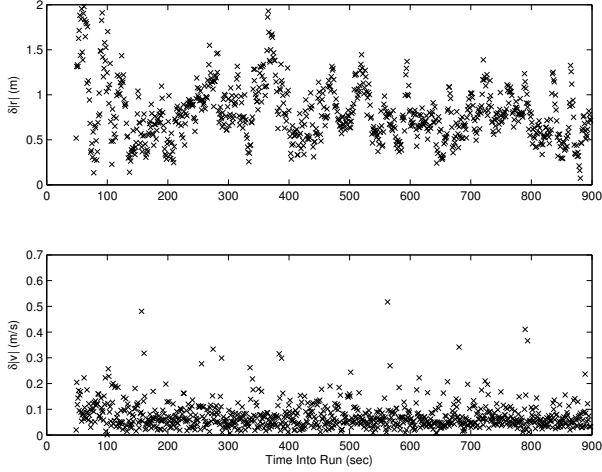


**Figure 11** FOTON Rectangular Track RMS Errors

observables provided by the simulator log file. This process is illustrated in Figure 12. Because atmospheric delays are not simulated, the pseudorange, carrier phase, and Doppler (pseudorange rate) observables consist of only range, range rate, receiver and SV clock errors, and a constant phase ambiguity (modulo one wavelength). The first difference is between the computed observables and the simulator log file for each SV; this removes all terms except for the receiver clock errors and the phase ambiguity. The resulting differences are then differenced again, removing the receiver clock errors. All that remains is the observable noise, assumed to be zero-mean Gaussian, and the phase ambiguity. Since the phase noise is much lower than one wavelength (about 19 cm), the mean of the phase double difference, modulo one wavelength, can be subtracted out to obtain the zero-mean Gaussian phase error.

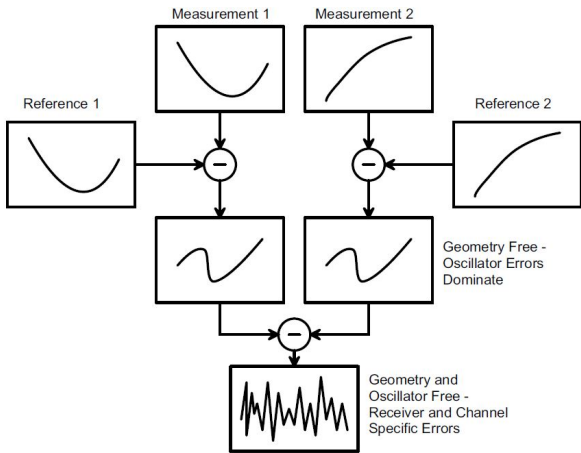


**Figure 12** Observable Double Difference [8]

Note that it does not actually matter if the receiver-simulator differences are made first, or if the SV-SV differences are made first. However, in this analysis it will be assumed that the receiver-simulator differences are first, followed by an SV-SV difference. As an example, the carrier phase double difference is outlined below:

$$\begin{aligned} \Delta\Phi^j &= \Phi_{rx}^j - \Phi_{sim}^j \\ &= c\delta t_r + \lambda N^j + n_{\Phi}^j \end{aligned} \quad (1)$$

$$\begin{aligned} \Delta\Phi^k &= \Phi_{rx}^k - \Phi_{sim}^k \\ &= c\delta t_r + \lambda N^k + n_{\Phi}^k \end{aligned}$$

$$\begin{aligned} \nabla\Delta\Phi^{jk} &= \Delta\Phi^k - \Delta\Phi^j \\ &= \lambda(N^k - N^j) + n_{\Phi}^k - n_{\Phi}^j \end{aligned} \quad (2)$$

$$\begin{aligned} \sigma_{\nabla\Delta\Phi}^2 &= \sigma_{\Phi}^2 + \sigma_{\Phi}^2 \\ &= 2\sigma_{\Phi}^2 \end{aligned} \quad (3)$$

Here,  $\Phi = \lambda\phi$  is the carrier phase expressed in meters,  $N^j$  and  $N^k$  are the integer phase ambiguities of SVs  $j$  and  $k$ , respectively, and  $n_{\Phi}^j$  and  $n_{\Phi}^k$  are the observable noise terms. Note that it is assumed here that the simulator noise is negligible compared to that of the receiver, and that the receiver noise is independent of SV, so that the double difference noise is a factor of  $\sqrt{2}$  greater than the actual observable noise.

The six SV pairs, along with the times in which both SVs are visible to the receiver, can be found in Ref. [8]. The results from the last double difference test are shown in Figure 13 as an example.

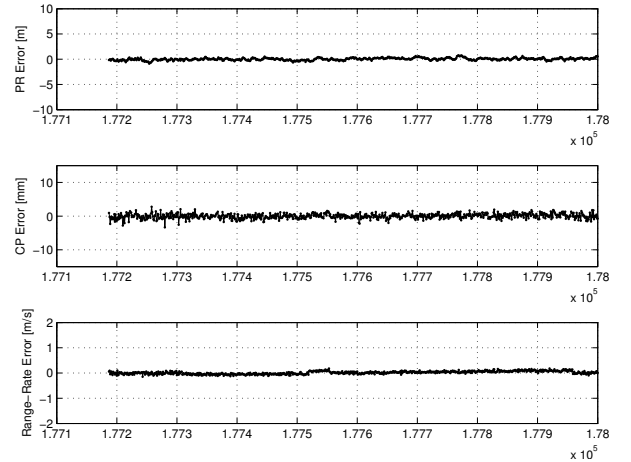


**Figure 13** SV 6-17 Double Difference After Time Tag Fix-up

The final test results are summarized in Table 2. Note that test 3 is not shown; this is because the simulator log file did not include one of the SVs required by

**Table 2** LEO Benchmark Testing Observables Noise

Test	Observable	FOTON	Architect	Orion	BlackJack	NovAtel
1	PR [m]	0.1455	0.9258	0.9477	0.1553	0.0991
	Phase [mm]	0.5286	0.9323	0.9253	0.5030	1.1970
	PR Rate [m/s]	0.0503	0.1407	0.1414	0.0010	0.0745
2	PR [m]	0.1449	0.9037	0.9193	0.1025	0.1121
	Phase [mm]	0.5734	0.9227	1.0890	0.4270	1.2567
	PR Rate [m/s]	0.0537	0.1382	0.1440	0.0010	0.0359
3	PR [m]	N/A	0.9015	0.9559	0.1323	0.1226
	Phase [mm]	N/A	1.0899	1.0699	0.4105	1.3715
	PR Rate [m/s]	N/A	0.1419	0.1561	0.0010	0.0351
4	PR [m]	0.1548	0.9131	0.9029	0.1539	0.1267
	Phase [mm]	0.6805	1.1566	1.6478	0.9524	1.3559
	PR Rate [m/s]	0.0649	0.1526	0.1512	0.0010	0.0426
5	PR [m]	0.1708	0.8986	0.8960	0.1606	0.1217
	Phase [mm]	0.5784	1.1864	1.7767	0.6380	1.3480
	PR Rate [m/s]	0.0552	0.1469	0.1473	0.0010	0.0565
6	PR [m]	0.1920	0.9297	0.8942	0.1242	0.1285
	Phase [mm]	0.6255	1.2112	1.5659	0.2833	1.4228
	PR Rate [m/s]	0.0605	0.1466	0.1534	0.0010	0.0401
Average	PR [m]	0.1616	0.9121	0.9193	0.1381	0.1185
	Phase [mm]	0.5973	1.0832	1.3458	0.5357	1.3253
	PR Rate [m/s]	0.0569	0.1445	0.1489	0.0010	0.0475

this test. Both SVs were simulated, as is evidenced by the fact that the receiver tracked both signals, however the log file only recorded a certain number of simulated SVs, and either SV 3 or 15 was not recorded between 177400 and 178900 seconds. This table shows that FOTON’s performance is a significant improvement over the Architect and Orion receivers, though not quite as good as the BlackJack or NovAtel. These receivers, however, likely use time averaging of observables to improve performance, a technique not currently implemented on FOTON.

#### 4 ON-ORBIT ACQUISITION AND REACQUISITION

In order to use FOTON on small satellites such as CubeSats, it is necessary to duty cycle the receiver due to power consumption constraints. While FOTON runs on an average of 4.5 W [12], a typical CubeSat has a total power budget of less than 10 W; it would not be feasible to use half of the total power for a single sensor. By only running FOTON for 1/3 of the time, however, its orbit-average power consumption can be reduced to 1.5 W. Since the receiver will only be active for short periods of time, it must be able to quickly acquire signals and begin reporting navigation solutions as soon as it is turned on. This section examines the time it takes to track enough signals to

compute a navigation solution (time to first fix). In addition, several loss-of-signal scenarios are examined to show FOTON’s signal reacquisition capabilities.

The scenario consists of the same polar LEO simulation used in the benchmark tests of section 3. During the simulation, six events simulate various types of signal loss or duty cycling; each event is separated by several minutes of tracking to allow the receiver to fully recover a position solution. First, 6 minutes into the simulation, the simulated spacecraft performs a slow (6 minute duration) 360° roll. Next, the antenna is detached for 60 seconds, then reattached. Another roll is performed when the spacecraft is near the north pole (2 minute duration). The next two events are system resets, followed by a complete system reboot.

The six events are illustrated in Figure 14 as gaps in the navigation solution. Note the large increase in residuals for the 360° rolls (the 1st and 3rd events); this is due to the gradual degradation of receiver-satellite geometry during the rolls.

##### 4.1 Time to First Fix

The time to first fix is the time it takes for the receiver to obtain a valid navigation solution, measured from the moment the receiver is turned on. Time to first

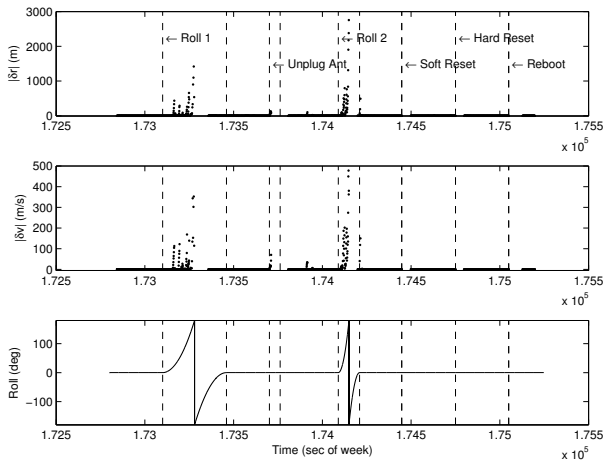


**Figure 14** Acquisition Simulation Residuals

fix varies depending on DOP and acquisition search depth, but on average, FOTON’s time to first fix is about 45-50 seconds.

#### 4.2 Six Minute Roll

The six minute roll began 5 minutes into the simulation. As can be seen in Figure 14, the receiver did not undergo a constant roll rate, but rather a more realistic spin-up and spin-down roll, with an average rate of 1 deg/sec. The receiver lost the navigation solution 185 seconds into the roll, and lost track of the last signal 200 seconds into the roll. In reality, the receiver could no longer see signals at at 180 seconds into the roll, because this was the half-way point when it was earth-pointing. However, the receiver continues to attempt to track signals that have disappeared until their low signal level identifies them as “ghost signals”. FOTON reacquired the first signal on the later half of the roll at 211 seconds into the roll, that is, 31 seconds after the antenna was earth-pointing. The first valid navigation solution was obtained 47 seconds later; the total gap between valid navigation solutions was approximately 73 seconds.

#### 4.3 Antenna Disconnect

Sudden loss of all signals was simulated by disconnecting the coaxial cable that connected the simulator to the receiver. This was done at a simulation time of 15 minutes, 3 minutes after the completion of the previous event. This 3 minute buffer ensured that the receiver had returned to normal operation. After the cable was disconnected, the receiver continued to track ghost

signals for 20 seconds before they were all “pruned”. After 60 seconds, the cable was reattached, and the receiver began tracking signals again 2 seconds later. A valid navigation solution was obtained 44 seconds later.

#### 4.4 Two Minute Roll

The two minute roll was started 21.5 minutes into the simulation, 5.5 minutes after the previous event. This time was chosen so that the receiver would be approximately at the north pole at the time of the roll, so that in addition to the roll dynamics, the satellite geometry would be challenging as well. Because this roll was much quicker than the previous one (3 deg/sec average), the receiver never actually lost track on all satellites. It tracked ghost signals until real ones became visible. However, there was a 50 second gap in the navigation solution, from 1 minute into the roll (when the antenna was earth-pointing) to 10 seconds before the end of the roll. Even with the faster roll, however, the receiver still recovered a valid navigation solution before the roll was complete.

#### 4.5 Soft and Hard Resets

Two reset commands can be issued to FOTON’s DSP: a soft reset and a hard reset. Although this structure makes room for future functionality, at present both commands are exactly the same, and hereafter will be referred to simply as a reset. The next two events, again separated by 5 minutes to allow the receiver to fully recover, were a soft and hard reset, respectively. As expected, both commands performed the same DSP reset, and took the same amount of time. It took 17-18 seconds from the time the command was issued to regain tracking of the first signal, and another 30 seconds after that until the first valid navigation solution. The antenna-disconnect event demonstrated that the receiver only takes a few seconds to actually acquire a signal, so the reset time is then approximately 14-15 seconds.

#### 4.6 SBC Reboot

Whereas the soft and hard resets only reset the DSP, a reboot actually shuts down the DSP and reboots the SBC (single board computer). The reboot was commanded 5 minutes after the second DSP reset, and took about 46 seconds until the first signal was tracked,

and another 32 seconds until the first navigation solution. Allowing 15 seconds for the DSP to reset, it takes about 30 seconds for the SBC to reboot. The SBC, however, would be replaced by a satellite's on-board computer, so the SBC reboot time has no bearing on FOTON's reset time.

#### 4.7 Summary

FOTON's DSP only takes about 15 seconds to reset, after which it immediately begins acquiring new signals. Allowing 30 seconds for ephemeris retrieval from the nav message, the time to first fix is still under one minute. This time can be further reduced by storing ephemerides in memory, and by running the DSP in low-power mode to reduce the time it takes to reset. With these modifications, the time to first fix can be reduced to just a few seconds, maximizing the amount of useful on-duty time.

### 5 KALMAN FILTER-BASED PRECISE ORBIT DETERMINATION

The results presented until now have used a standard least-squares iterative solution based on the pseudorange and Doppler observables from each tracked SV [13]. In static scenarios, these basic point solutions can be averaged to improve overall precision. Similarly in dynamic scenarios, an Extended Kalman Filter (EKF) can be used to incorporate a time history of observables into a more precise navigation solution. This section outlines a basic orbital EKF for FOTON that improves on the default point solutions, making possible on-board, sub-meter precise orbit determination (POD) after a sufficient improvement of the dynamics model fidelity.

#### 5.1 State Dynamics

The receiver's state consists of Earth-Centered, Earth-Fixed (ECEF) position  $\mathbf{r}$  and velocity  $\mathbf{v}$ , and clock bias  $\delta t_R$  and rate  $\delta \dot{t}_R$ :

$$\mathbf{x} = \begin{pmatrix} \mathbf{r} \\ c\delta t_R \\ \mathbf{v} \\ c\delta \dot{t}_R \end{pmatrix} \quad (4)$$

where the speed of light  $c$  is used to express the clock terms in equivalent meters and meters per second (for unit consistency with the position and velocity states).

The receiver clock bias is defined as the difference between the receiver time and true GPS time (TGT):

$$\delta t_R = t_R - t_{GPS} \quad (5)$$

This EKF will be based on true GPS time rather than receiver time, so all time derivatives will be with respect to TGT.

The state differential equation model is then

$$\mathbf{f} = \dot{\mathbf{x}} = \begin{pmatrix} \mathbf{v} \\ c\delta \dot{t}_R + u_t \\ \mathbf{a} + \mathbf{u}_v \\ u_f \end{pmatrix} \quad (6)$$

where  $\mathbf{a}$  is the total acceleration in the ECEF frame, and  $\mathbf{u}_v$ ,  $u_t$ , and  $u_f$  are uncorrelated, zero-mean, white-noise processes with covariances given by

$$\mathbf{Q}_v = E[\mathbf{u}_v \mathbf{u}_v^T] = \sigma_v^2 \mathbf{I}_{3 \times 3} \quad (7)$$

$$\sigma_t^2 = E[u_t(t)u_t(\tau)] = \frac{1}{2} h_0 c^2 \delta(t - \tau) \quad (8)$$

$$\sigma_f^2 = E[u_f(t)u_f(\tau)] = 2\pi^2 h_{-2} c^2 \delta(t - \tau) \quad (9)$$

Here,  $h_0$  and  $h_{-2}$  are constant parameters (units of sec and  $\frac{1}{\text{sec}}$ , respectively) used to characterize a receiver's clock stability [14], and  $\delta(t - \tau)$  is the Kronecker delta function (units of  $\frac{1}{\text{sec}}$ ). The velocity process noise  $\sigma_v$  will serve as a filter tuning parameter.

The ECEF acceleration term in Equation 6 can be expressed in terms of the ECI acceleration:

$$\mathbf{a} = \mathbf{g} + 2\omega_e \begin{pmatrix} v_y \\ -v_x \\ 0 \end{pmatrix} + \omega_e^2 \begin{pmatrix} x \\ y \\ 0 \end{pmatrix} \quad (10)$$

where  $\mathbf{g}$  is the total acceleration in the ECI reference frame. For now, a simple J2 gravity model [15] will be used, with no atmospheric drag. For a full derivation, including linearization and covariance propagation, see Ref. [16].

#### 5.2 Measurement Models

This orbital EKF uses pseudorange and pseudorange rate observables in its measurement updates. While the pseudorange is a raw observable, the pseudorange rate is not; it is derived from Doppler. Since the only difference between pseudorange rate and Doppler is a constant scaling, however, the pseudorange rate is treated as a raw observable.

##### *Pseudorange*

The pseudorange model consists of the true range  $r^k$  to the  $k$ th SV, the receiver clock bias  $\delta t_R$ , the SV clock bias  $\delta t_S^k$ , tropospheric  $T^k$  and ionospheric  $I^k$  delays, and noise  $n_\rho^k$ :

$$\hat{\rho}_k = r^k + c(\delta t_R - \delta t_S^k) + I^k + T^k + n_\rho^k \quad (11)$$

The noise in the pseudorange measurement can be estimated as a function of signal carrier-to-noise ratio  $C/N_0$ :

$$\sigma_\rho^2 = \frac{dB_{DLL} T_c^2 c^2}{2 \frac{C}{N_0}} [m^2] \quad (12)$$

where  $d = \frac{t_{\text{eml}}}{T_c}$  is the DLL correlator's early-minus-late chip spacing,  $T_c$  is the chip length (1 ms for GPS L1 C/A), and  $B_{DLL}$  is the DLL bandwidth in Hz.

### Pseudorange Rate

The pseudorange rate is derived from the Doppler observable as follows:

$$\dot{\rho} = -\lambda f_D = -c \frac{f_D}{f_0} \quad (13)$$

Where  $f_0$  and  $\lambda$  are the L1 frequency and wavelength, respectively, and  $f_D$  is the observed Doppler shift of the received signal. The negative sign is introduced because the Doppler shift is positive for approaching SVs, when the range rate is negative. A model for the pseudorange rate based on the current state involves the relative velocity  $v_r$  along the line-of-sight vector  $\ell$ , the receiver clock rate  $\delta \dot{t}_R$ , and the satellite clock rate  $\delta \dot{t}_S$ :

$$\hat{\rho} = \left[ \frac{c \delta \dot{t}_R - c \delta \dot{t}_S - v_r (1 + \delta \dot{t}_S)}{(1 + \delta \dot{t}_S)(c + v_r)} \right] c \quad (14)$$

where  $v_r$  is the line-of-sight velocity, or the negative of the range rate.

The noise in the pseudorange rate measurement can be estimated from carrier phase noise, a function of  $C/N_0$ , PLL bandwidth  $B_n$ , and the accumulation interval  $T_{acc}$  (part of the squaring loss  $S_L$  term).

$$\sigma_\phi^2 = \frac{B_n}{\frac{C}{N_0} S_L} \text{ rad}^2 \quad (15)$$

$$S_L^{-1} = 1 + \frac{1}{2 T_{acc} \frac{C}{N_0}} \quad (16)$$

Doppler can be approximated with a single-difference of phase, which leads to the pseudorange rate noise

estimate.

$$f_D = -\frac{\dot{\rho}}{\lambda} \approx \frac{\phi_2 - \phi_1}{2\pi T_{acc}} \quad (17)$$

$$\dot{\rho} \approx -\frac{\lambda}{2\pi T_{acc}} (\phi_2 - \phi_1) \quad (18)$$

$$\sigma_{\dot{\rho}}^2 \approx \frac{2\sigma_\phi^2 \lambda^2}{(2\pi T_{acc})^2} \quad (19)$$

$$\sigma_{\dot{\rho}}^2 \approx \frac{2\lambda^2 B_n}{\frac{C}{N_0} S_L (2\pi T_{acc})^2} \text{ m}^2/\text{sec}^2 \quad (20)$$

### 5.3 EKF Results

The EKF was tested using the same polar LEO simulation as in previous sections. The EKF is initialized with the first point solution obtained (about 45 seconds into the simulation), with a diagonal initial covariance, with  $\sigma_{r0} = \sigma_{t0} = 0.5 \text{ m}$  and  $\sigma_{v0} = \sigma_{f0} = 0.1 \text{ m/s}$ . These values are based on the approximate noise apparent in the standard point-wise navigation solution. The filter was tuned by varying the velocity process noise  $\sigma_v$ ; the value that produced the best results was  $\sigma_v = 0.001 \text{ m/s}^2$ . The clock noise terms were calculated using  $h_{-2} = 2.9 \times 10^{-21} \text{ sec}^{-1}$  and  $h_0 = 3.4 \times 10^{-21} \text{ sec}$ ; these parameters were empirically computed by Kassas and Pesyna of the Radionavigation Laboratory for the TCXO used in FOTON's RF front end.

The position residuals are shown in Figure 15. Although the EKF noticeably reduces the noise in the position solution as compared with the point-wise solutions, it does not reduce the overall bias. This is because the EKF gravity model only includes J2 effects, whereas the simulator used a 10th order gravity model. The velocity, on the other hand, is nearly zero-mean, with an order-of-magnitude reduction of noise.

There is no way to directly measure clock error, so the best that can be done is to compare the clock bias and rate with the values obtained by the point-wise solutions computed at the same time. The difference in bias and rate (in equivalent meters and meters per second) is shown in Figure 16. It should be noted, however, that most of the noise shown is from the point solution; this can be seen in Figure 17, which shows the point-wise and EKF solutions for the clock rate. The EKF solution has much lower noise than the point solution. The results of the EKF vs. point solution comparison are summarized in Table 3.

**Table 3** EKF and Point-Wise Residuals

Solution Type	Position [m]		Velocity [m/s]		Clock	
	Mean	Std	Mean	Std	Bias	Rate
EKF	0.174	0.544	$1.22 \times 10^{-4}$	0.0121	0.432 m	0.157 m/s
Point	0.122	0.739	0.0812	0.247	N/A	N/A

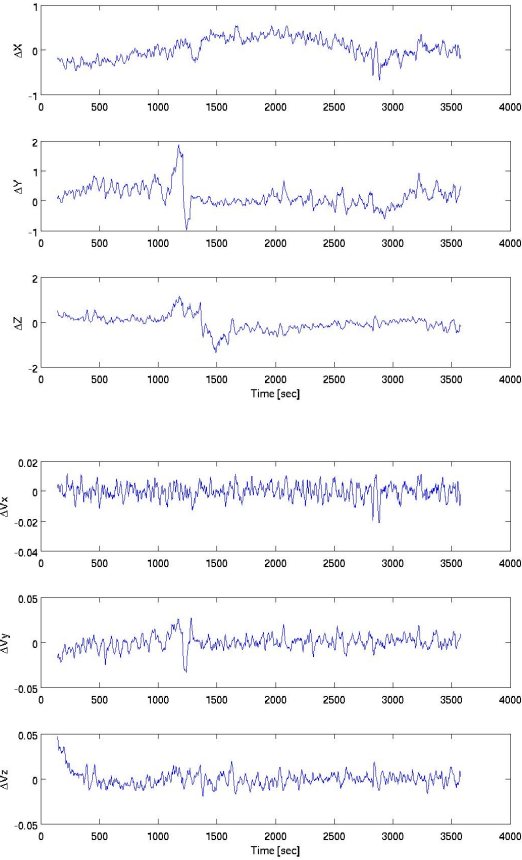


**Figure 15** EKF Position and Velocity Residuals

## 6 DUAL-FREQUENCY CAPABILITY

Designed specifically to be an ionospheric sensor, the CASES receiver was already set up to process dual-frequency measurements. Although FOTON will also use its dual-frequency capability to directly measure ionospheric delay during satellite occultations, this section will focus on using the L2C signal to negate the effect of ionospheric delays to improve the navigation solution.

The Spirent simulator at UT-Austin that was used in previous tests is incapable of simulating L2C signals, so it could not be used for dual-frequency testing. Fortunately, Cornell University, one of the collaborators on the CASES receiver, has a newer Spirent device

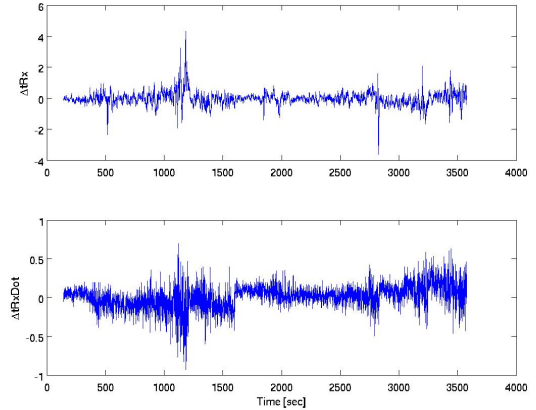


**Figure 16** EKF - Point Solution Clock Residuals

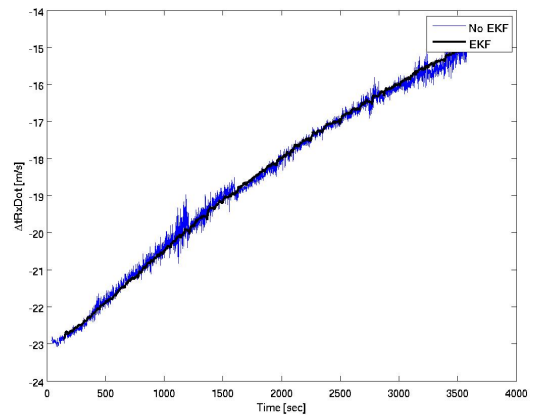


**Figure 17** EKF  $c\delta t_R$  Solution

that does simulate L2C. O’Hanlon of Cornell used the newer simulator to record a dual-frequency, LEO simulation similar to the previously tested baseline polar orbit. In this simulation, L2C was simulated on all satellites. Currently, there are only 9 L2C-capable GPS satellites on orbit; however, the limited number of L2C-capable satellites can still be simulated by specifying in FOTON’s configuration file which satellites to attempt to track. Also note that the simulated ionosphere was based on the standard Klobuchar model.

## 6.1 Dual-Frequency Ionospheric Delay Estimation

Most dual-frequency receivers directly eliminate the ionospheric delay for L2C-capable SVs by forming a measurement known as the “ionosphere-free” pseudorange:

$$\begin{aligned}\tilde{\rho}_{L1} &= \rho_{L1} - \frac{f_{L2}^2}{f_{L2}^2 - f_{L1}^2}(\rho_{L1} - \rho_{L2}) \\ &= \frac{f_{L1}^2 \rho_{L1} - f_{L2}^2 \rho_{L2}}{f_{L1}^2 - f_{L2}^2}\end{aligned}\quad (21)$$

FOTON, however, does not use this ionosphere-free pseudorange. Instead, it uses the L1 and L2 pseudoranges from L2C-capable SVs to update a running estimate of vertical TEC (TECV). Satellite elevation is then used to map the TECV to a slant TEC for L1-only SVs as well as L2C-capable SVs. Not only does this method improve the estimate of ionospheric delay for L1-only satellites as well as L2C-capable ones, but it also acts as a filter on the ionospheric delay estimates, reducing noise. This works very well for stationary receivers (such as FOTON’s predecessor CASES), but it may present problems for LEO receivers. For instance, while TECV changes slowly for stationary receivers, it will change more rapidly for LEO receivers. In this case, independent, point-wise estimates of ionospheric delay may be more accurate, albeit more noisy, than filtered estimates.

## 6.2 LEO Simulation Testing

Once the interfrequency bias was determined, FOTON was tested using four different configurations. The baseline configuration (case 1) tracked L1 only, and initialized the Klobuchar model parameters with the actual parameters used in the simulation (also in the broadcast ephemeris). By initializing the Klobuchar parameters with the values used in the simulator from the beginning of the simulation, the receiver’s ionospheric model is exactly matched with the simulator’s model. This baseline case, then, should be more accurate than even dual-frequency configurations. Case 2 also tracked L1 only, but it initialized the Klobuchar parameters with the default null values; this demonstrates the receiver’s default single-frequency performance in the presence of ionospheric delays. Case 3 tracked L1 and L2 on all satellites. This shows what performance can ultimately be expected as the GPS constellation is modernized. Case 4 also tracked L1 and L2, but restricts the L2 signals tracked to the 9 PRNs that currently transmit L2C. The results here

presented were from the standard point-wise navigation algorithm; each case was also tested with the Kalman filter, but due to the low-fidelity dynamics model, sub-meter precision was not attained.

The position residuals from the case 1 are shown in Figure 18. Note the increase in noise near the end of the simulation; this was when the receiver was passing over the north pole, so DOP was higher.

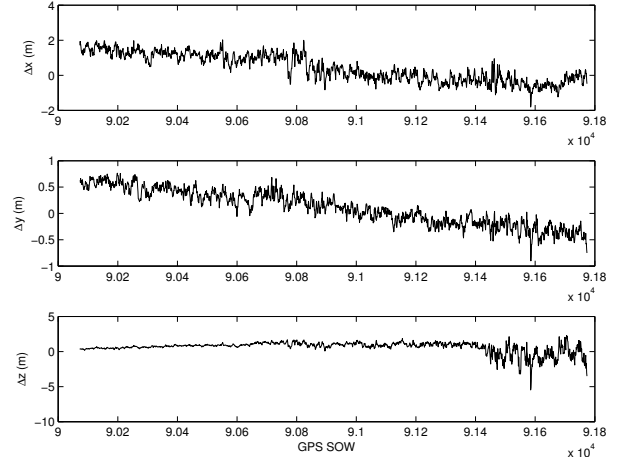


**Figure 18** Position Residuals, L1-Only, Initialized Klobuchar Model (Case 1)

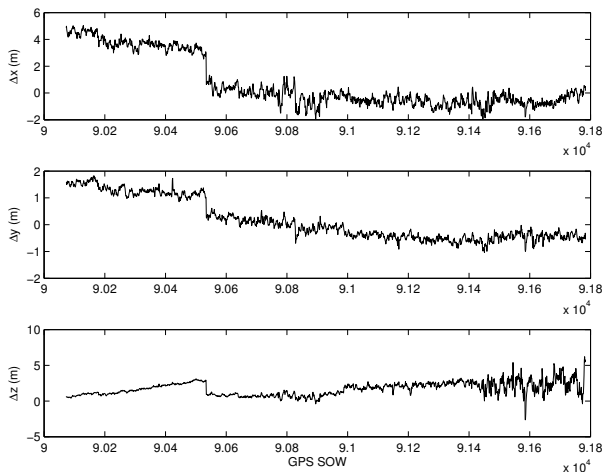
Comparing this with case 2 (Fig. 19), the position residuals for the single-frequency configuration with uninitialized Klobuchar parameters, reveals a large initial error that is corrected about 8 minutes into the simulation. In this configuration, the Klobuchar model is initialized with null parameters, so the estimated ionospheric delay is zero. Once the Klobuchar parameters have been received from the broadcast ephemeris, however, the model is updated, and the ionospheric delays are properly estimated. After this correction, the residuals follow the same trends as the baseline configuration.

The position residuals for case 3 are shown in Figure 20. As expected, the errors are very similar to the baseline configuration (Fig. 18). Because of the way FOTON filters the L2C measurements to estimate the ionospheric delay for L1-only SVs as well as L2C-capable ones, the reduction in performance in case 4 (with limited number of L2C signals tracked) is minimal (Fig. 21).

Table 4 summarizes the position and velocity residuals for all four configurations. As expected, the best configuration was the baseline; however, this is only because the receiver exactly matched ionospheric models with the simulator. The first half of case 2 is more

**Table 4** Position and Velocity Point Solution Residuals

	Position [m]		Velocity [m/s]	
	Mean	1- $\sigma$	Mean	1- $\sigma$
L1, Init. Params	0.7650	1.1520	0.0657	0.3035
L1, Uninit. Params	1.8520	2.2786	0.0661	0.3094
DF, All L2C	1.1040	1.4711	0.0628	0.2920
DF, Limited L2C	1.1190	1.2749	0.0612	0.3048

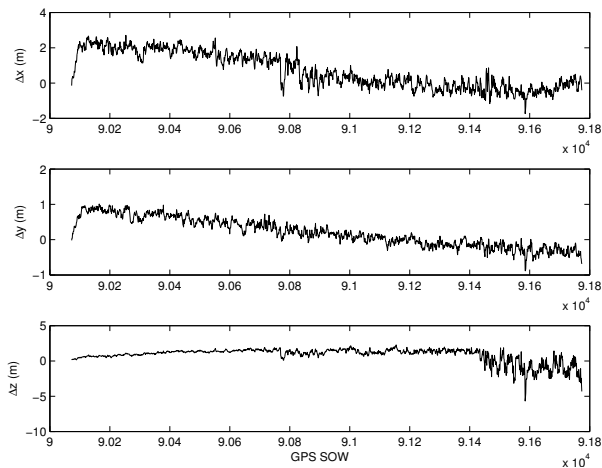
**Figure 19** Position Residuals, L1-Only, Uninitialized Klobuchar Model (Case 2)

representative of single-frequency performance. The two dual-frequency configurations were nearly identical; this is because of the filtering method currently employed to estimate the ionospheric delays. Note that the velocity residuals for all four configurations are essentially the same. This is because the standard point-wise navigation algorithm used in these tests computes velocity using Doppler only, and is independent of pseudorange, and thus ionospheric delay.

A comparison of these results with the single-frequency test results of Chapter 3 reveals a degradation in performance. This is clearly due to the presence of ionospheric delay on the pseudorange. However, sub-meter accuracy of the dual-frequency solutions is still attainable by including the raw L2 pseudorange in a Kalman filter that is designed to process dual-frequency measurements. This capability, however, has yet to be developed.

## 7 RADIO OCCULTATION OBSERVATION

In most terrestrial scenarios, GPS signals are received from relatively high elevation. In these cases, the signals travel through the ionosphere and troposphere

**Figure 20** Position Residuals, Dual-Frequency, All L2C (Case 3)

more or less perpendicularly, passing through all of the layers before reaching the receiver. If the receiver is in LEO, however, it can track signals below the horizon; this happens as GPS satellites set behind the LEO satellite, because its velocity is much higher than that of the semi-synchronous GPS satellites. When this occurs, signals pass horizontally through the ionospheric and tropospheric layers (Fig. 22); such an event is known as an occultation.

By using dual-frequency measurements, the slant total electron count (STEC or just TEC) along the signal path during an occultation can be directly computed. As the SV sets, the signal travels through more layers of the ionosphere, and the TEC increases. Complete TEC profiles during occultations can be used to map the ionosphere and monitor space weather. At low enough elevations, delay through the troposphere can also be calculated and used to compute density profiles, which can then be used to improve terrestrial weather models.

Several missions have been devoted entirely to radio occultations. The currently-operational COSMIC mission, for example, uses a small constellation of satellites with high-precision GPS receivers to observe occultations world-wide [3]. With the small, low-power

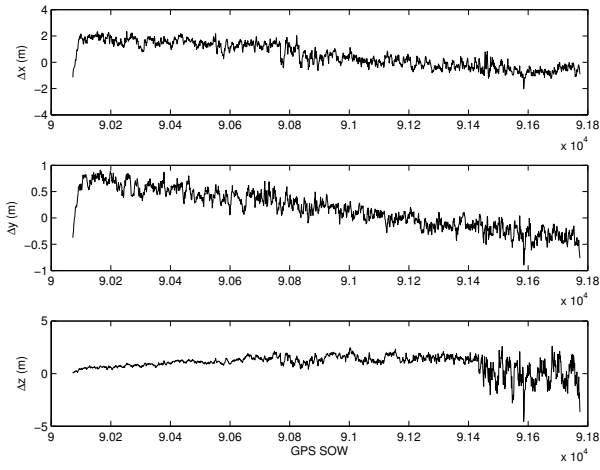


**Figure 21** Position Residuals, Dual-Frequency, Limited L2C (Case 4)

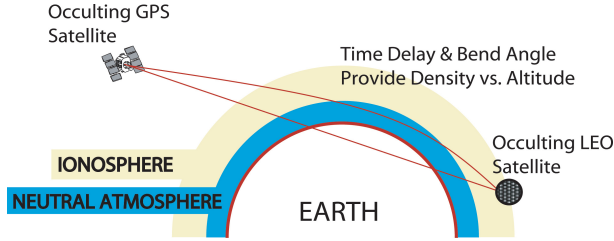


**Figure 22** Radio Occultation [3]

FOTON receiver, a similar mission could be performed with a larger constellation of much smaller CubeSats. Such a mission would provide even greater world-wide coverage than COSMIC at a fraction of the expense.

### 7.1 Occultation Observation in a LEO Simulation

The dual-frequency LEO simulation from section 6 contains a number of occultations of varying elevations. To illustrate FOTON’s occultation observing capability, the lowest-elevation SV tracked, PRN 13, was analyzed. FOTON acquired PRN 13 at an elevation of  $78^\circ$ , and tracked it until it set at an elevation of  $-15^\circ$ . The slant TEC, computed with the pseudorange measurements, is the noisy measurement shown in Figure 23. The carrier-phase-derived TEC is the smooth line in this figure. Note, however, that carrier-phase-derived TEC is ambiguous, so it must be appropriately shifted to yield an accurate TEC measurement. If the pseudorange-derived TEC is denoted as  $TEC_\rho$  and the carrier-phase-derived TEC relative to zero is denoted as  $\delta TEC_\Phi$ , then the unbiased carrier-phase-

derived TEC, denoted  $TEC_\Phi$ , is computed as

$$TEC_\Phi(t) = \delta TEC_\Phi(t) + E[TEC_\rho(t) - \delta TEC_\Phi(t)] \quad (22)$$

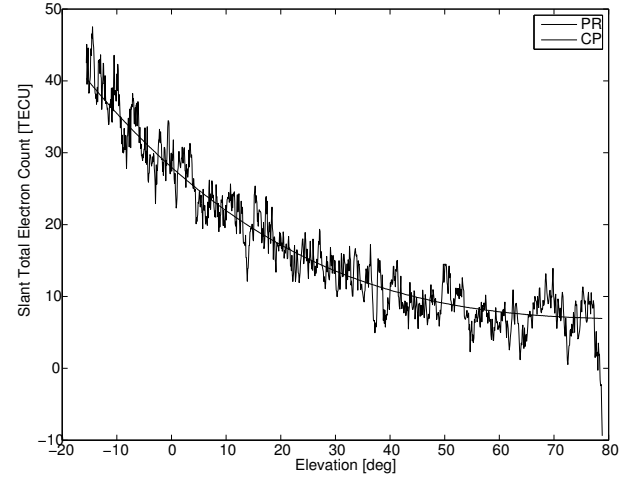


**Figure 23** Slant TEC versus Elevation

Assuming a spherical Earth and a straight signal path through the ionosphere, the lowest altitude attained by the signal can be computed from the elevation as follows:

$$h_{min} = r \cos(el) - R_e \quad (23)$$

where  $r$  is the norm of the LEO satellite’s position,  $R_e$  is the Earth’s mean equatorial radius, and  $el$  is the occulting SV’s elevation. Note that these are not very good assumptions; the Earth is better modeled with an equatorial bulge, and the signal is bent as it travels through the ionosphere. However, these simplifying assumptions allows the elevation in Figure 23 to be mapped to altitude, shown in Figure 24, which illustrates that FOTON was able to track PRN 13 until it was blocked by the Earth itself.

This short example demonstrates that FOTON can be used effectively as an occultation sensor, even aboard a CubeSat. The relatively small expense of FOTON, combined with its small size and low power requirements, could make large-scale CubeSat occultation missions feasible.

## 8 HIGH ALTITUDE AND GEOSYNCHRONOUS ORBITS

Up to this point, testing and development of FOTON has been based on the assumption that the receiver

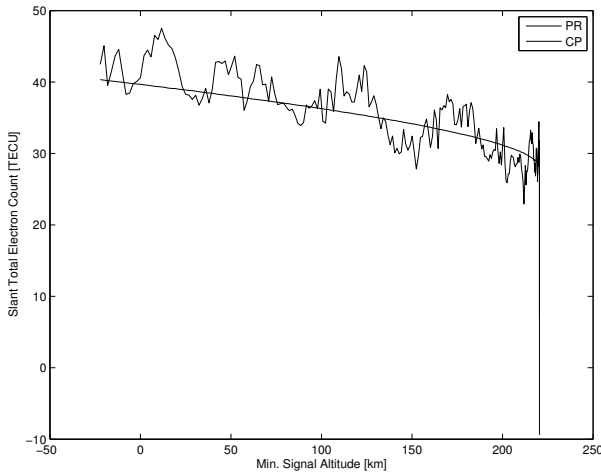


Figure 24 Slant TEC versus Altitude

is in LEO. However, many satellites are placed in high Earth orbits (HEO), particularly geosynchronous (GEO). With a semi-major axis of 42164 km, GEO satellites are well outside the GPS constellation. Although GPS signals are directed toward the earth, the transmitters were designed with a slightly wider beam than is necessary for Earth coverage; as a result, a receiver in HEO or even GEO can still see some signals that are not blocked by the Earth (Fig. 25). In addition, the GPS transmitting antenna gain pattern includes some lower-power side lobes that may be possible to track. This section presents the results of preliminary GEO testing of the FOTON receiver.

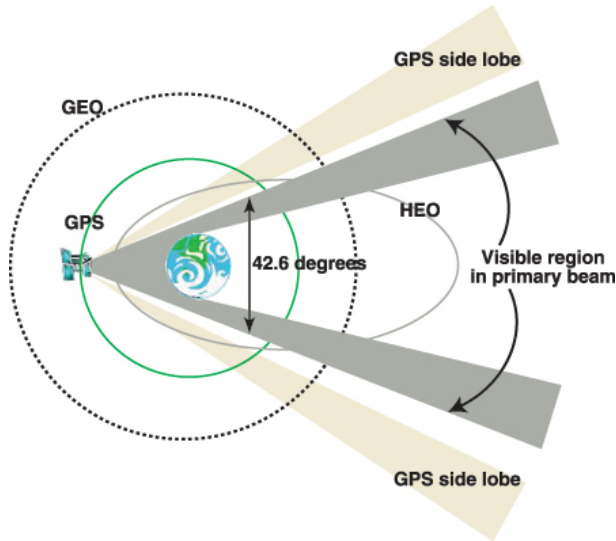


Figure 25 HEO/GEO GPS Geometry [17]

## 8.1 GEO Simulation Setup

One challenge in setting up a GEO simulation is that, by default, the Spirent simulator assumes an isotropic transmitting antenna. This simplifying assumption is inconsequential for terrestrial or even LEO simulations, but it is unacceptable for GEO. Fortunately, the simulator is adaptable enough to allow the user to input a gain pattern for the transmitting antennae. The gain pattern used in the simulation is shown in Figure 26.

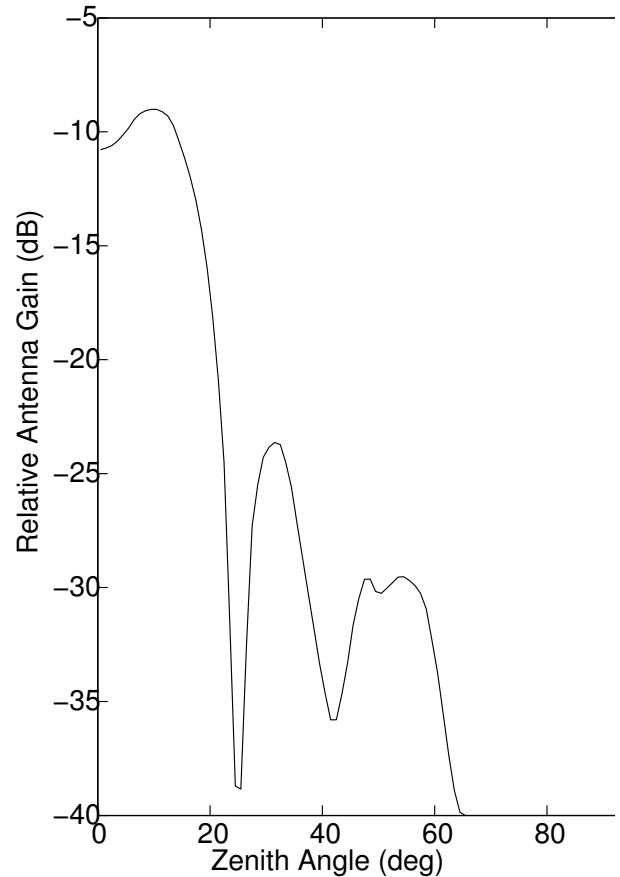


Figure 26 GPS Transmitting Antenna Gain Pattern [18]

As demonstrated by Moreau, the number of GPS satellites visible to a receiver in HEO/GEO is only occasionally four or more. Due to data storage limitations, a complete 24-hour simulation was not practical; instead, the GPS ephemerides for a specific epoch (in this case, week 1139, 172800 seconds of week) were propagated for 24 hours, and a two-hour window containing at least four visible satellites was selected. This window began at 244800 seconds of week 1139.

Unlike the previous tests in which FOTON used its

own internal TCXO clock, this time the receiver was slaved to an external OCXO. This more stable clock allows a reduction in the PLL bandwidth, which decreases the signal noise. This increases the received  $C/N_0$ , which is essential to tracking weak signals in GEO.

## 8.2 Point-Wise Solutions

In order to acquire and track the weak signals expected in GEO, FOTON was configured to perform 20 ms coherent accumulation; this is the maximum allowable accumulation interval without using data bit wipe-off techniques. In addition, the Doppler search window was reduced to  $\pm 10$  kHz because the receiver is expected to be stationary (in the ECEF frame). Finally, the PLL bandwidth was also reduced to 10 Hz, further decreasing noise levels.

As anticipated, the receiver tracked four signals for most of the two-hour simulation. The number of satellites tracked is shown in Figure 27; it varied from two to four SVs. During the times when the receiver

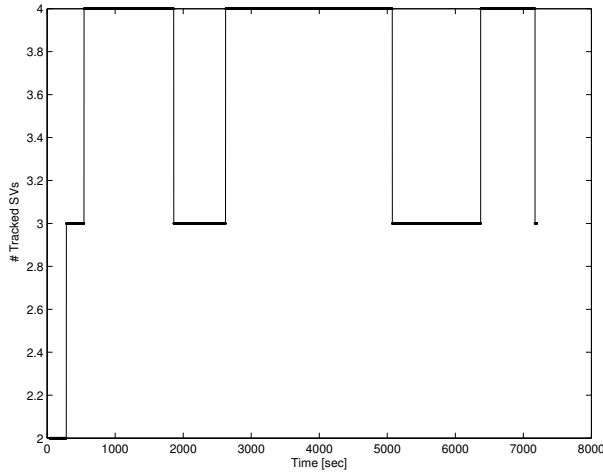


**Figure 27** Number of Satellites Tracked

tracked four satellites it was able to compute a navigation solution using the standard point-wise algorithm. Given the fact that DOP is one to two orders of magnitude higher in GEO, the residuals of these point solutions are relatively small (Fig. 28).

The already bad geometry appears to get even worse towards the end of the simulation (after 5000 seconds), but for the first two periods of four-SV-visibility, the navigation solution is relatively good. The error along the X-axis (the radial direction) is far worse than the errors in the Y-Z horizontal plane. This is no surprise

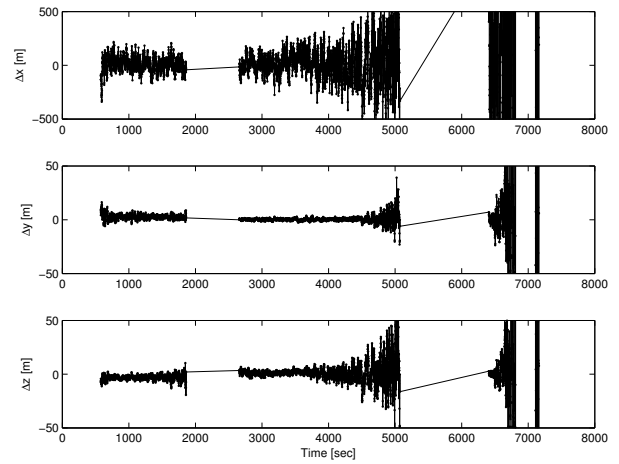


**Figure 28** GEO Position Residuals

given the lack of geometric diversity in the X-direction. The errors for these first two data sets are given in Table 5.

**Table 5** GEO Navigation Solution Residuals

	X	Y	Z	$\ r\ $
	Position [m]			
Mean:	18.281	1.276	-0.145	18.326
1- $\sigma$ :	155.3673	3.1213	7.9116	155.5999
	Velocity [m/s]			
Mean:	2.3692	0.3665	0.1286	2.4008
1- $\sigma$ :	14.92136	0.26513	0.68159	14.93927

## 8.3 Summary

By using an external OCXO to allow smaller a PLL bandwidth and using longer coherent accumulation time to increase signal  $C/N_0$ , FOTON is able to determine horizontal position in GEO to within 10 meters, and vertical position within 200 meters, without the need of filtering. A properly tuned Kalman filter would further enhance performance. Furthermore, due to the low signal dynamics present in GEO, even longer coherent accumulation times may be used, provided the data bits are wiped off appropriately. This will allow FOTON to pull in signals from transmitter side lobes in addition to the main lobes, making more SVs visible, and further increasing GEO navigation performance.

## 9 CONCLUSION

As satellites shrink in size and grow in navigation requirements, the need for a small, low-power, dual-frequency, space-based GPS receiver becomes evident. As a software-defined receiver, FOTON has great potential for meeting this need.

Low Earth orbit single-frequency simulations show that 0.5 m precision orbit determination is attainable by FOTON, with potential for better performance using a Kalman filter. Dual-frequency LEO simulations yield 1.5 m precision in the presence of ionospheric delays; this could also be improved by implementing a Kalman filter that processes raw dual-frequency measurements rather than ionosphere-corrected single-frequency measurements.

With a time to first fix of approximately 45 seconds, FOTON could be duty-cycled to conserve power. For example, operating a total of 8 hours per day, it would consume 1.5 W orbit average power instead of 4.5 W. FOTON could operate less frequently if needed by relying on a high-fidelity Kalman filter to make up for the fewer measurements. Because FOTON is a software-defined receiver, such settings could be changed on-orbit.

Another advantage of FOTON's versatility as a software-defined receiver is that, with slight modifications to its configuration file and using an external OCXO as a timing reference, FOTON can navigate in geosynchronous orbits. Tracking signals from the GPS transmitting antenna main lobe, FOTON is able to navigate within 10 m horizontal and 200 m vertical precision. With some additional modifications, such as data bit wipe-off and long coherent accumulation, FOTON should also be able to track signals from the first side lobe. This would allow FOTON to track more than four SVs, further increasing navigation precision.

In addition to FOTON's potential for precise orbit determination in LEO and GEO, it could also be developed into a radio occultation sensor. Capable of tracking signals down to the surface of the Earth, FOTON could be modified to map tropospheric as well as ionospheric profiles during occultations. This would allow such missions as COSMIC to be performed at a fraction of the cost.

## REFERENCES

- [1] <http://www.csr.utexas.edu/grace/>. Accessed November 21, 2011.
- [2] <http://fastrac.ae.utexas.edu>. Accessed November 21, 2011.
- [3] <http://www.cosmic.ucar.edu/>. Accessed November 21, 2011.
- [4] T. Humphreys, M. Psiaki, and P. Kintner. GNSS Receiver Implementation on a DSP: Status, Challenges, and Prospects. In *2006 ION GNSS Conference*, September 2006.
- [5] B. O'Hanlon, M. Psiaki, S. Powell, J. Bhatti, T. Humphreys, G. Crowley, and G. Bust. CASES: A Smart, Compact GPS Software Receiver for Space Weather Monitoring. In *2011 ION GNSS Conference, 2011*, 2011.
- [6] D. Bobyn. L1/L2 GPS Receiver Front End Hardware Technical Description. Technical report, Cornell University, 2010.
- [7] B. O'Hanlon, M. Psiaki, P. Kintner, and T. Humphreys. Development and Field Testing of a DSP-Based Dual-Frequency Software GPS Receiver. In *2009 ION GNSS Conference*, 2009.
- [8] G. Holt. Benchmark Testing for Spaceborne Global Positioning System Receivers. Master's thesis, The University of Texas at Austin, May 2002.
- [9] G. Holt, E. G. Lightsey, and O. Montenbruck. Benchmark Testing for Spaceborne Global Positioning System Receivers. In *2003 AIAA GNC Conference*, August 2003.
- [10] <http://radionavlab.ae.utexas.edu>. Accessed November 21, 2011.
- [11] <http://spaceflight.nasa.gov/realdata>. Accessed March 1, 2011.
- [12] FOTON Sensor Preliminary Specifications. Technical report, The University of Texas at Austin, 2010.
- [13] P. Misra and P. Enge. *Global Positioning System - Signals, Measurements, and Performance*. Ganga-Jamuna Press, Lincoln, MA, 2nd edition, 2006.
- [14] M. Psiaki. Satellite Orbit Determination Using a Single-Channel Global Positioning System Receiver. *Journal of Guidance, Control, and Dynamics*, 25(1):137–144, 2005.
- [15] B. Tapley, B. Schutz, and G. Born. *Statistical Orbit Determination*. Elsevier Academic Press, 2004.

- [16] A. Joplin. Development and Testing of a Miniaturized, Dual-Frequency, Software-Defined GPS Receiver for Space Applications. Master's thesis, The University of Texas at Austin, December 2011.
- [17] <http://www.gpsworld.com>. Accessed November 16, 2011.
- [18] F. Czopek and S. Shollenberger. Description and Performance of the GPS Block I and II L-Band Antenna and Link Budget. In *1993 Institute of Navigation Conference*, 1993.